

865 ern hemisphere coolings: a salt source for the glacial Atlantic? *Earth and
Planetary Science Letters*, 245, 39–55.

WAIS Divide Project Members (2015). Precise interpolar phasing of abrupt
climate change during the last ice age. *Nature*, 520, 661–665.

Weaver, A. J., Eby, M., Wiebe, E. C., Bitz, C. M., Duffy, P. B., Ewen, T. L.,
870 Fanning, A. F., Holland, M. M., MacFadyen, A., Matthews, H. D. et al.
(2001). The UVic Earth System Climate Model: Model description, climatol-
ogy, and applications to past, present and future climates. *Atmosphere-Ocean*,
39, 361–428.

Wunsch, C. (2006). Abrupt climate change: An alternative view. *Quaternary
875 Research*, 65, 191–203.

7. Supplementary Material A: Locations of ocean sediment cores

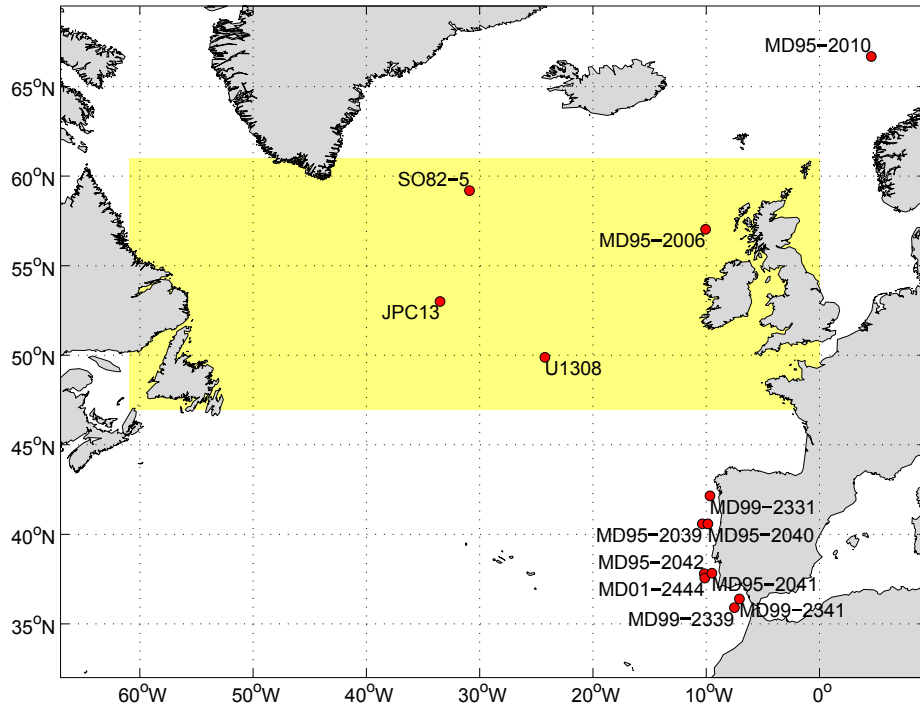


Figure 9: Locations of ocean sediment cores. Yellow color indicates the area where freshwater is added in our simulations.

8. Supplementary Material B: Surface atmospheric temperature, precipitation and $\delta^{18}\text{O}$ precipitation response

The results of an EOF analysis of surface atmospheric temperature (SAT), precipitation, and $\delta^{18}\text{O}$ precipitation are shown in Figure 10. Their corresponding principal component time series are in a very close agreement with changes in AMOC, with stronger anomalies during large freshwater events and weaker anomalies during small freshwater events (Figure 10D). In addition, changes in atmospheric CO_2 concentrations are the dominant EOF mode for atmospheric temperatures (Figure 10E).

Stadial conditions are characterized by cooling over the North Atlantic and Eurasian regions (Figure 10A), with strongest amplitudes found over Northern Europe. Warming is simulated over the North Pacific, North America, and

890 at high southern latitudes. The meridional temperature seesaw is the result
of AMOC-driven changes in northward heat transport in the Atlantic and is
consistent with other modelling studies (e.g. Stouffer et al., 2006; Timmermann
et al., 2010; Kageyama et al., 2013; Menviel et al., 2015) and paleoproxy records
(Blunier et al., 1998; Barker et al., 2009; Stenni et al., 2011). The seesaw con-
895 nection between the North Atlantic and the North Pacific is associated with
changes in North Pacific Deep Water (NPDW) formation in agreement with
earlier studies (Saenko et al., 2004; Okazaki et al., 2010; Menviel et al., 2011;
Huiskamp & Meissner, 2012; Bagniewski et al., 2015).

900 The North Atlantic cooling reduces evaporation which in turn leads to drier
conditions over the North Atlantic, with highest amplitudes along the 60°N
parallel (Figure 10B). As discussed by Stouffer et al. (2006); Clark et al. (2007)
and Lee et al. (2011), cooling in the North Atlantic enhances the meridional sur-
face pressure gradient, displacing the Intertropical Convergence Zone towards
905 the Southern Hemisphere. This results in a southward shift of the tropical rain-
bands, extending from South America into the equatorial Africa, and can be seen
as a dipole pattern in Figure 10B. Stadial conditions are further characterized
by a decrease in $\delta^{18}\text{O}$ precipitation, centered in the Greenland Sea (Figure 10C).

910 An EOF mode associated with atmospheric CO_2 variability explains a signif-
icant portion of the variance in surface atmospheric temperature (SAT) (73.08%,
Figure 10E) and precipitation (26.47%, Figure 10F). Atmospheric CO_2 increase
during Heinrich stadials is associated with an increase in precipitation in the
North Pacific and the Southern Ocean, thus contributing to the North At-
915 lantic/South Atlantic and North Atlantic/North Pacific seesaw patterns, as has
been previously demonstrated, e.g. by Timmermann et al. (2010) for the South-
ern Ocean.

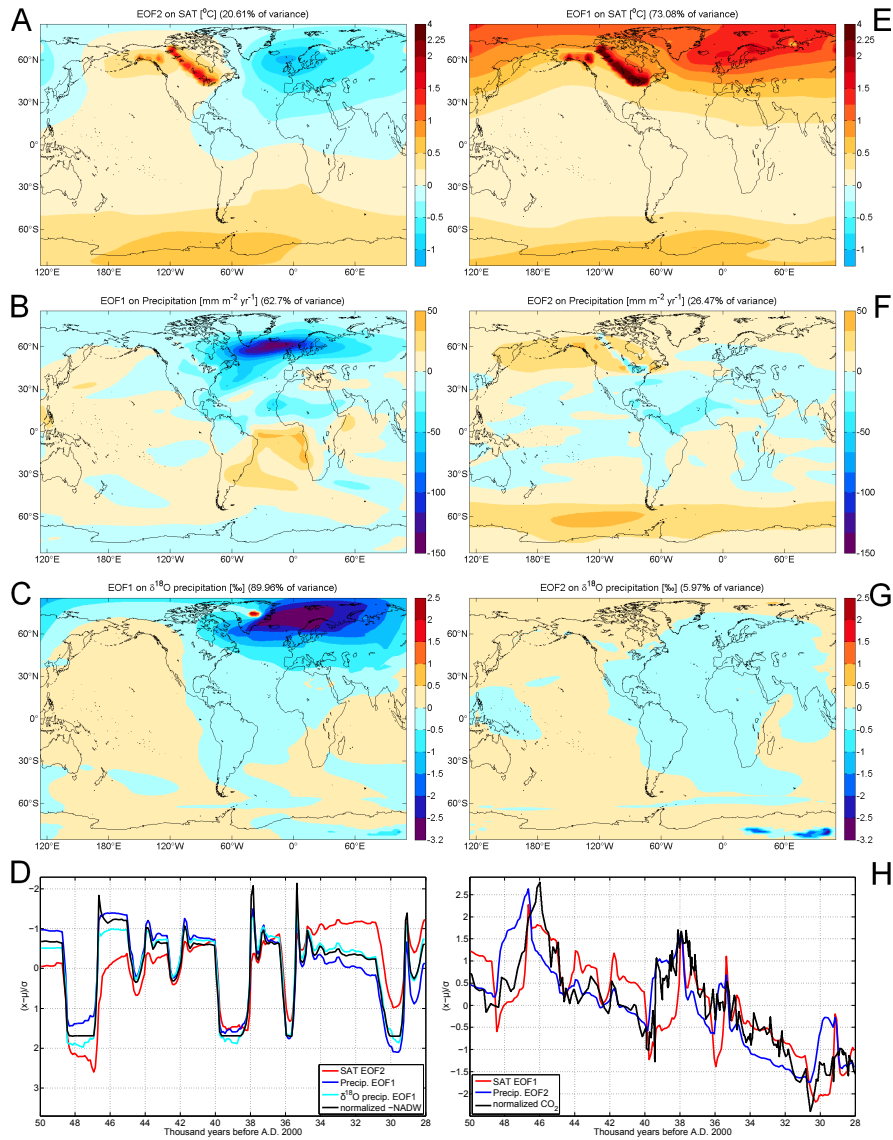


Figure 10: (A) Pattern of second EOF of surface atmospheric temperature (SAT) anomalies ($^{\circ}\text{C}$), which explains 21% of the variance; (B) Pattern of first EOF of precipitation anomalies ($\text{mm m}^{-2} \text{yr}^{-1}$), which explains 63% of the variance; (C) Pattern of first EOF of detrended $\delta^{18}\text{O}$ precipitation anomalies ($\%$), which explains 90% of the variance; (D) normalized principal components of second EOF of surface atmospheric temperature (SST, red), first EOFs of precipitation (Precip., blue) and $\delta^{18}\text{O}$ precipitation ($\delta^{18}\text{O}$ precip., cyan), and normalized North Atlantic Deep Water formation rate (NADW, black); (E) Pattern of first EOF of surface atmospheric temperature (SAT) anomalies ($^{\circ}\text{C}$), which explains 73% of the variance; (F) Pattern of second EOF of precipitation anomalies ($\text{mm m}^{-2} \text{yr}^{-1}$), which explains 26% of the variance; (G) Pattern of second EOF of detrended $\delta^{18}\text{O}$ precipitation anomalies ($\%$), which explains 6% of the variance; (H) normalized principal components of first EOF of surface atmospheric temperature (SST, red) and second EOF of precipitation (Precip., blue), and normalized North Atlantic Deep Water formation rate (NADW, black). Please note that the y axis and the normalized NADW time series in Figure 10D have been reversed.